Supporting Information:

Concentration and Velocity Profiles in a Polymeric Lithium-ion Battery Electrolyte

Hans-Georg Steinrück,[1,2,3,*,+] Christopher J. Takacs,[1,2,*,+] Hong-Keun Kim,[4,5] David M. Mackanic,[6] Benjamin Holladay,[7] Chuntian Cao,[1] Suresh Narayanan,[8] Eric M. Dufresne,[8] Yuriy Chushkin,[9] Beatrice Ruta,[9,10] Federico Zontone,[9] Johannes Will,[11] Oleg Borodin,[12] Sunil K. Sinha,[7] Venkat Srinivasan,[4,5] and Michael F. Toney[1,2,13,*]

[1]SSRL Materials Science Division, SLAC National Accelerator Laboratory, Menlo Park, California 94025, USA
[2]SLAC National Accelerator Laboratory, Joint Center for Energy Storage Research (JCESR), Lemont, Illinois 60439, USA
[3]Department Chemie, Universität Paderborn, 33098 Paderborn, Germany
[4]Argonne National Laboratory, Lemont, Illinois 60439, USA
[5]Argonne National Laboratory, Joint Center for Energy Storage Research (JCESR), Menlo Park, California 94025, USA
[6]Department of Chemical Engineering, Stanford University, Stanford, California 94305, USA
[7]Department of Physics, University of California, San Diego, La Jolla, California 92093-0319, USA
[8]X-ray Science Division, Argonne National Laboratory, Lemont, Illinois 60439, USA
[9]ESRF – The European Synchrotron, 71 avenue des Martyrs, 38043 Grenoble, France
[10]Universté Lyon, Universitè Claude Bernard Lyon 1, CNRS, Institut Lumière Matière, Villeurbanne, France.
[11]Institute of Micro- and Nanostructure Research (IMN) & Center for Nanoanalysis and Electron Microscopy (CENEM), University of Erlangen-Nuremberg, Germany
[12]Energy Storage Branch, Sensor and Electron Devices Directorate, U.S. Army Research Laboratory, Adelphi, MD 20783, USA
[13]Department of Chemical and Biological Engineering, University of Colorado, Boulder, CO 80309, USA

*: hans.georg.steinrueck@uni-paderborn.de, ctakacs@slac.stanford.edu, michael.toney@colorado.edu
[+]: Equal contribution

1. Methods

A. Electrolyte preparation

Anhydrous acetonitrile was purchased from Sigma Aldrich and used without further purification. High purity Lithium bistrifluoromethanesulfonimidate (LiTFSI) was purchased from Sigma Aldrich; prior to utilization, LiTFSI was dried under vacuum in a Schlenk line at 120°C for 2 days. Poly(ethylene oxide) (PEO) with an average molecular weight of 600000 kg/mol was purchased from Sigma Aldrich, and dried for 7 days under vacuum at room temperature. All following procedures were performed in an Ar-filled glovebox. To prepare the LiTFSI/PEO electrolyte at r = 0.1 (r corresponds to molar ratios between Li ion and ethylene oxide monomer unit), 816 mg of LiTFSI and 1250 mg of PEO were mixed in 13 ml of acetonitrile in a Teflon vial. This mixture was stirred using a Teflon coated magnetic stir bar at 300 rpm for 3 days at room temperature. Subsequently, acetonitrile was evaporated at room temperature for approximately 72 hours, after which the solution was heated to 90 °C for several days to remove any excess solvent. This procedure reproducibly yielded minimal amount of vapor bubbles trapped within the LiTFSI/PEO electrolyte.

B. Electrochemical cell preparation and electrochemistry

A schematic drawing of the *operando* electrochemical cell is depicted in Figure S1. A photograph in the assembled state and the copper heating block is also shown in Figure S1. The channel length was chosen as 3 mm, the channel diameter as 1 mm, and the window thickness as 2 mm for each window. The latter choice was motivated by the optimal scattering ratio between sample and window material of 1:1 for heterodyne velocity measurements (see below). All following procedures were performed in an Ar-filled glovebox. To fill the electrolyte channel, the PEEK frame was first heated to 90 °C; subsequently, the electrolyte was extruded into the 1 mm channel using 1/4-28 Teflon HPLC plugs. After this procedure, leftover electrolyte was cleaned from the flat-bottom sections of both sides of the cell via scrapping at room temperature. Subsequently, Li metal was attached by self-adhesion to the stainless-steel electrodes; before interfacing the Li electrodes with the electrolyte; Li metal was scrapped using Teflon tweezers until visibly shiny. The electrodes were then brought in contact with the electrolyte via screwing in HPLC nuts, which press the electrodes against the flat bottom (see Figure S1). Finally, the cells were sealed using 5 min epoxy, and annealed at 90 °C for at least 8 hours prior to XPCS measurements.

All electrochemical experiments were performed at 90 °C. Constant voltage polarization at 0.3 V was performed using a Biologic SP-150 potentiostat.

C. X-ray photon correlation spectroscopy

X-ray photon correlation spectroscopy (XPCS) measurements in the small-angle scattering regime were performed at beamline 8-ID-I [1] at The Advanced Photon Source (APS) and at beamline ID10 at the ESRF. The X-ray energy was 11 keV and 8.1 keV, respectively. The beamsize was 15 (horizontal) by 15 (vertical) µm and 10 by 15 µm, respectively, with a primary beam intensity of 2.36e[9] and 1.02e[11] photons/second, respectively, with speckle contrast of 11 and 24%, respectively. The detector was a LAMBDA detector (55 µm square pixels) at a distance of 3930 mm and a Maxipix 2x2 pixel detector (55 µm square pixels) at a distance of 5240 mm, respectively. This resulted in a measured q-range of $q_{\min} = 0.0029\ \text{Å}^{-1}$ and $q_{\max} = 0.0192\ \text{Å}^{-1}$ and $q_{\min} = 0.0006\ \text{Å}^{-1}$ to $q_{\max} = 0.0108\ \text{Å}^{-1}$, respectively, where $\mathbf{q} = \mathbf{k}_{\text{out}} - \mathbf{k}_{\text{in}}$

is the scattering vector and $\mathbf{k}_{\mathrm{in,out}}$ are the wave vectors of the incoming and scattered beam. A beamstop directly in front of the detector was used to block the primary beam.

XPCS scans were performed by reading out the detector at a frequency of 0.06 sec 6000 times (at APS), yielding a total of 360 seconds per XPCS scan. While the system is dynamic within the 360 sec timescale, the changes are minor (few percent), leading us to the conclusion that each XPCS scans represents a snapshot of the electrochemical state. The correlation function was calculated via two time correlation function using Hadoop Map Reduce [2, 3] on a distributed computing cluster. During the XPCS scans, the beam was attenuated by a factor of 16 to minimize radiation damage. To verify that the correlation functions were not affected by beam-induced dynamics, correlation functions were calculated for the first 1/10$^{\mathrm{th}}$s and last 1/10$^{\mathrm{th}}$s of the XPCS scan. If these matched, this showed that beam–induced dynamics are negligible. In addition, we performed this analysis for a series of attenuation-levels, and typically chose the absorber that was 2x higher than the absorber for which the previous analysis held true. After each XPCS, scan the sample was translated by at least 50 µm. This procedure yielded measurements with reproducibility.

XPCS measures the time dependence of the coherent scattering pattern [4, 5], i.e. speckle pattern, from a sample, and accordingly probes the system density fluctuations about equilibrium. In optical mixing techniques, we generally distinguish between homodyne and heterodyne techniques. In traditional optical laser dynamic light scattering (DLS) in homodyne mode, only the scattered light impinges on the detector, whereas in heterodyne technique, a small portion of the unscattered laser light is mixed with the scattered light [6] before detection. One of the advantages of heterodyne mixing is that absolute information about the uniform velocity of scatterers can be obtained. Equivalent conditions can be achieved in the DLS X-ray analogue XPCS via inserting a static reference scatterer of intensity $I(q)_{\mathrm{static}}$ into the coherence volume which also contains the fluctuating sample which exhibits a scattering intensity $I(q)_{\mathrm{dynamic}}$. Accordingly, XPCS can also be utilized to measure absolute velocities via employing heterodyne mixing [7, 8]. We note that the sign of the velocity, however, cannot be measured, as explained below.

Information on the dynamic structure factor is obtained by calculating the scattering vector dependent intensity-intensity auto-correlation function

$$g_2(\mathbf{q},\tau) = \frac{\langle I(\mathbf{q},t)I(\mathbf{q},t+\tau)\rangle}{\langle I(\mathbf{q})\rangle^2}$$

Equation 1

where $\langle\ \rangle$ denotes the time and pixel average, and τ is the delay time between XPCS frames. The intensity-intensity auto-correlation function provides insight into length scale dependent dynamic processes [9].

For a sample moving at constant velocity with respect to a static reference sample, and under the assumption that the dynamic and static sample are located within the coherence volume, the normalized correlation function yields the following expression [6, 7]

$$g_2(\mathbf{q},\tau) = 1 + \beta(1-h)^2 + h^2\beta e^{-2\left(\frac{\tau}{\tau_0(q)}\right)^{\gamma}} + 2h(1-h)\beta\cos\omega\tau\, e^{-\left(\frac{\tau}{\tau_0(q)}\right)^{\gamma}}$$

Equation 2

Here,

$$\omega = \mathbf{q}.\mathbf{v} = qv\cos\chi$$

Equation 3

where β is the coherence factor, $h = \frac{I(q)_{\mathrm{dynamic}}}{I(q)_{\mathrm{dynamic}}+I(q)_{\mathrm{static}}}$ is the heterodyne fraction, τ_0 is systems relaxation time, modelled to be a stretched exponential with stretching factor γ, $\mathbf{v}$ is the sample velocity vector, and χ is the angle between scattering and velocity vector (which is the azimuthal scattering angle, i.e. the angle between q_x and q_y, since the applied electric field imposes motion along the x-direction). Two extreme cases in terms of heterodyne fraction are apparent, i.e. $h \approx 0$ leads to a constant correlation function of magnitude $1+\beta$, and $h = 1$ leads to the typical homodyne correlation function of $g_2(\mathbf{q},\tau) = 1+\beta e^{-\left(\frac{2\tau}{\tau_0(q)}\right)}$. $I(q)_{\mathrm{dynamic}}$ should be of the same magnitude (i.e. ideally $h = 0.5$) as $I(q)_{\mathrm{static}}$ in order to maximize the velocity signal, i.e. the $\cos\omega\tau$ term.

The dependence of $g_2(\mathbf{q},\tau)$ on the azimuthal scattering angle necessitates the division of the detector into regions of constant q (within $q \pm \frac{\delta q}{2}$, with in our case $\delta q \approx 0.00097\ \mathrm{Å}^{-1}$) and constant χ (within $\chi \pm \frac{\delta\chi}{2}$, with $\delta\chi = 20°$), whereas in a typical XPCS experiments the correlation function for pixels within a given q-range are averaged regardless of χ. With $q_{\mathrm{min}} = 0.0029\ \mathrm{Å}^{-1}$ and $q_{\mathrm{max}} = 0.0192\ \mathrm{Å}^{-1}$, this yielded a total of 324 regions (see **Figure S2**). For each region, a single correlation function was calculated by averaging the correlation functions over the entire region size. In order to extract ion velocities from our *operando* XPCS data, the following data analysis pipeline (here explained for an exemplary dataset which is plotted in Fig. 2 in the main text) was performed (analogous to Refs. [8, 10]); the outlined steps (A) – (E) were performed for all datasets.

(A) All correlation functions were fit using **Equation 2**. This is shown for a representative dataset for $q = 0.038\ \mathrm{Å}^{-1}$ and for all 18 χ-values in **Figure S2**(a) (main text). All data sets are described well by the model. Fits were performed using in-house code implemented in the python LMFIT [11] environment, typically employing the differential evolution fit algorithm [11]. The heterodyne fraction h was initially varied, and then fixed at 0.7. While the scattering intensity changes slightly over time due to the varying ion concentration (see **Figure S3** and **Figure S4**), this procedure yielded reproducible fits. The value of h = 0.7 is also consistent with the transmission-corrected scattering intensities extracted for solely LiTFSI-PEO and solely PEEK (see **Figure S5**).

(B) Subsequently, the oscillation frequency ω in the g_2-function as a function of χ was fit using $\omega = |qv\cos\chi|$. This is illustrated in **Figure 2**(c) (main text), showing good agreement between data and model. From this fit, the velocity v was obtained. Note that this velocity nominally corresponds to a single q-value. Additionally, the good agreement between model and theory in **Figure 2**(c) suggest that, for a given q-value, the relationship $\omega = |qv\cos\chi|$ is valid, showing that we are indeed measuring a sample which moves at constant velocity.

(C) Further evidence is presented in **Figure 2**(b) (main text). Here, we present g_2-functions for which the time-delay x-axis was re-scaled according to **Equation 3** to $\tau\,|\cos\chi|$, plotted for the first nine q-value (this process required re-binning) [8, 10]. We note that at higher q-values the data were too noisy to yield significant improvements in the analysis. These data were subsequently fitted using **Equation 2**, yielding nine ω values. These are plotted as a function of q in **Figure 2**(d) (main text), showing a linear relationship with an abscissa and ordinate intercept at zero. This is the expected linear dependence and provides further proof that we are measuring a sample which moves at constant velocity.

(D) This q-dependence observation allowed us to collapse all the g_2-functions onto a common $q\tau\,|\cos\chi\,|$ axis (involving re-binning). This is shown **Figure 2**(e) (main text). Note that in this representation the oscillation period is directly inversely proportional to the constant velocity. We point out that the apparent possibility of applying the rescaling further suggests that τ_0 also scales with $1/q$. In this context, it must be noted in passing that the origin of τ_0 can also include contributions from a distribution of velocities within the beam (in addition to corresponding to the system's relaxation).

(E) Via this procedure, all 324 correlation functions can be mapped into a single master correlation function. In practice, the best signal to noise ratio in the rescaled g_2-functions was typically obtained for averaging for q-values up to 0.0067 Å^{-1}. The outlined procedure has two advantages. (1) It reduces the amount of fits necessary to obtain a velocity from 72 (for four q-regions) to a single fit, which (2) renders the fit results significantly more robust. Given that the velocity (and hence oscillation period) changes by almost an order or magnitude over the entire polarization series and position, the fitted range was accordingly adjusted to weight the portion of the correlation functions that show oscillations (in contrast to portions at larger $q\tau\,|\cos\chi\,|$ values where the oscillations are fully damped to just a flat baseline).

In order to spatially resolve the velocity across the 3 mm channel, we performed XPCS measurements at five locations within the channel as indicated in the inset of **Figure 6**(b) (main text) during polarization of the Li/PEO-LiTFSI/Li symmetric cell. We note that after mounting the cell in the beamline heating chamber (which was flushed with Helium during the experiment) and heating to 90 °C, XPCS measurements were collected until several measurements yielded identical results, showing that the system reached its equilibrium state. Equilibrium was typically reached after several hours. While the variation in velocity along x (direction from electrode to electrode) has physical meaning, the distribution in y and z (in the plane of electrodes) is irrelevant under the current conditions where the transport is a solely one-dimensional problem. **Figure S6** shows the location of each measurement point in the cell, along with the electrochemical polarization times. While measurements closer to the channel edges are desirable, these were not possible in the current cell design due to window geometry.

Finally, it is worth pointing out that while XPCS allows us to measure the direction of the velocity vector, our analysis of the correlation functions does not allow us to unravel the sign of the velocity vector. While this can in principle be determined via visible inspection of the speckle movement [7], this was not possible in our case due to the lack of scattering intensity. This implies that we cannot distinguish between a sample moving from the left to the right (or positive to negative electrode), versus a sample moving from the right to the left (but we can distinguish left-to-right from up-to-down).

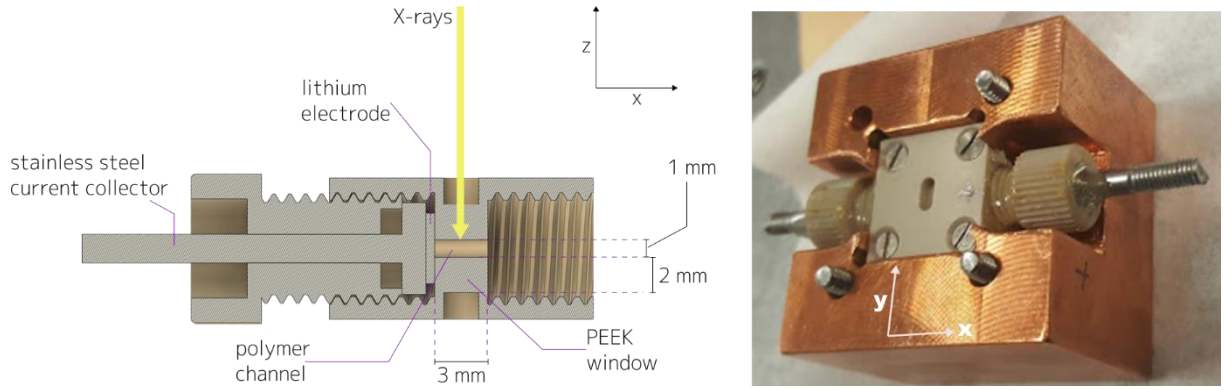

Figure S1: Schematic and photograph of *operando* XPCS cell. In the schematic, the lithium electrode was only inserted in one side of the cell.

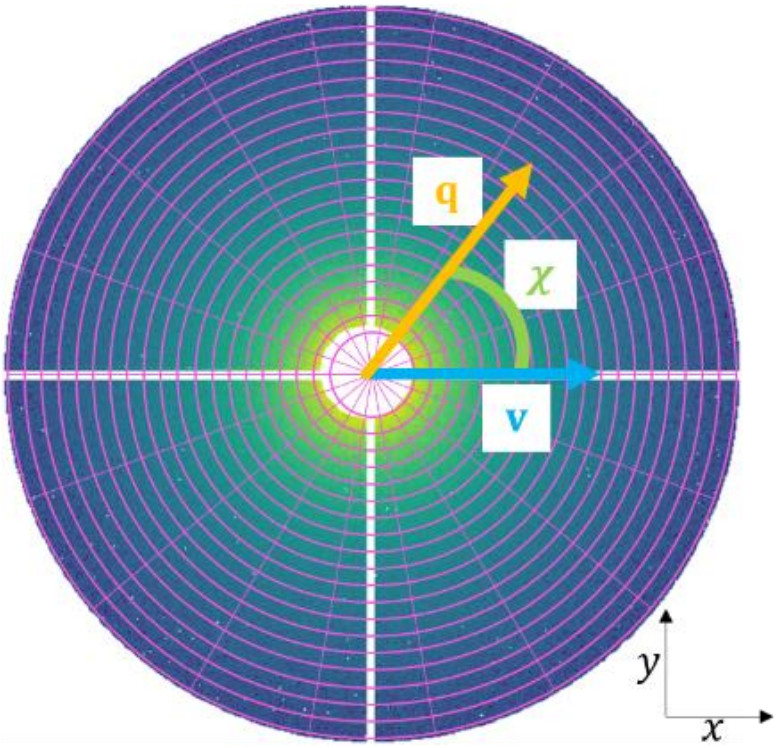

Figure S2: 2D small angle X-ray scattering pattern within the analyzed portion of the detector. The radial/azimuthal bins indicate the regions within which correlation functions were averaged that then correspond to a single q-χ combination.

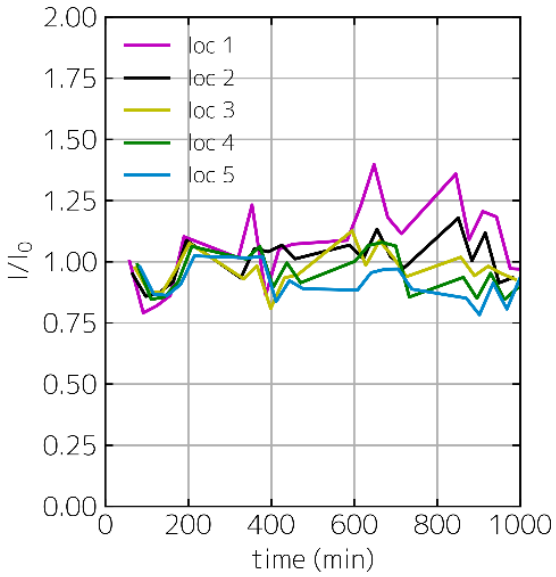

Figure S3: Transmission corrected mean scattering intensity (within $0.005 < q < 0.010$ Å^{-1}) for the five different locations as a function of polarization time (color-code corresponding to Figure 5 (main text)). We observe a trend in which the scattering intensity increases for decreasing ion concentration, whereas the scattering intensity decreases for increasing ion concentration. As the ion concentration changes with time, the time dependence of the scattering intensity is related to the concentration dependence of the scattering intensity. It is worth noting that the observed behavior also rules out that the scattering originates from trace impurities in the samples, in which case one would expect unchanged scattering intensities over time.

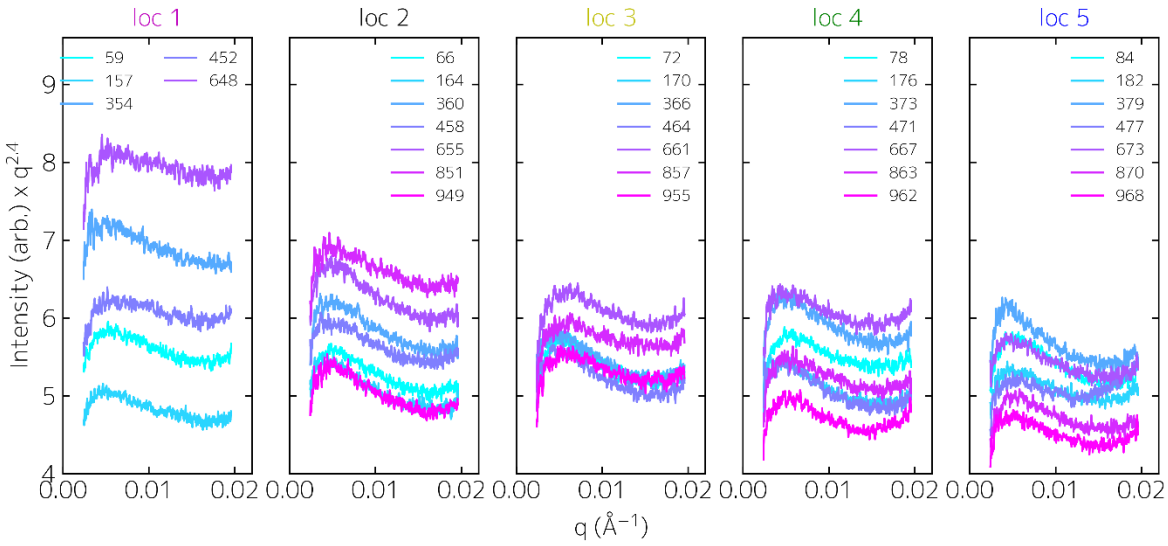

Figure S4: Transmission corrected small angle X-ray scattering for the five different locations as a function of time (scaled by $q^{2.4}$ to highlight the differences).

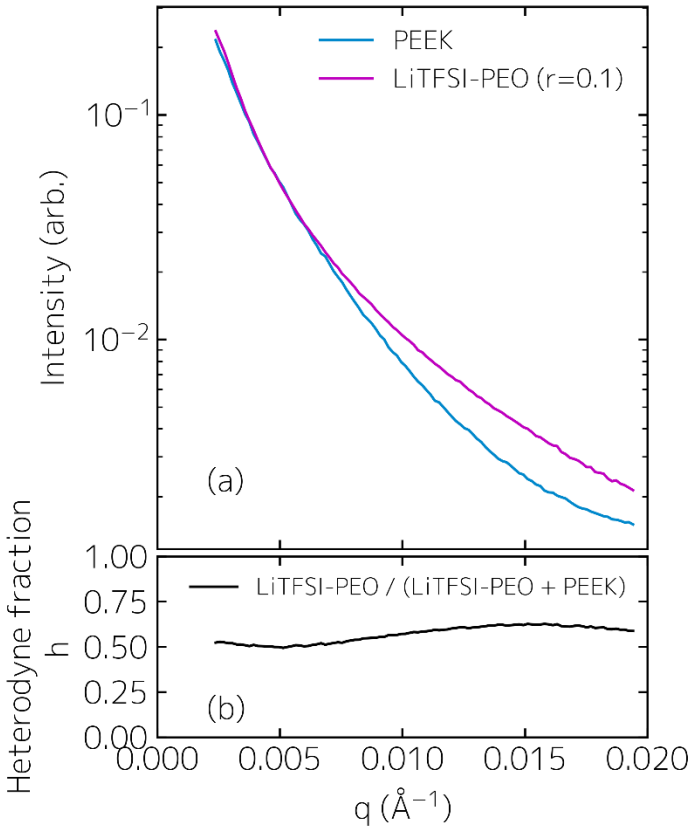

Figure S5: Transmission-corrected X-ray scattering intensity of pure LiTFSI-PEO and PEEK (a), as well as their ratio, which corresponds to the heterodyne fraction $\boldsymbol{h}$ (b).

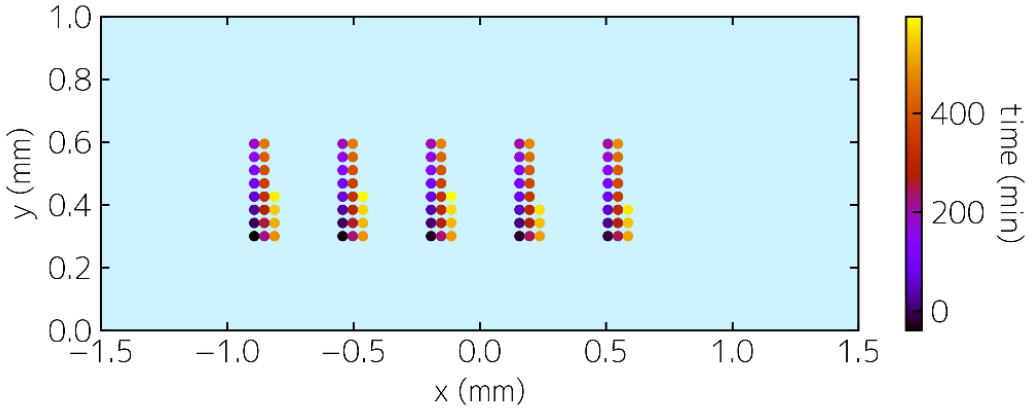

Figure S6: Illustration of locations measured via XPCS as a function of polarization time.

D. X-ray absorption microscopy

The concentration profiles were obtained via X-ray scanning absorption microscopy (XAM), i.e. by scanning the 3 mm channel (see **Figure S1**) in x-direction across the 15 x 15 µm beam. At each position x along the channel, we measure the intensity transmitted through the sample (I_T) (the incoming X-ray intensity (I_0) was calculated from the known PEEK absorption coefficient). $TFSI^-$ is the main x-ray absorbing component in the cell. With this knowledge we can calculate the concentration of $TFSI^-$ via its known absorption cross section and Lambeert-Beer's law, $I_\mathrm{T} = I_0 e^{-\mu t}$; here μ is the attenuation coefficient for $TFSI^-$, and t is the depth of the channel along the beam path, i.e. 1 mm. This concentration measurement was performed after every five XPCS scans, i.e. at a frequency of about 30 minutes. In practice, this analysis also requires the incorporation of the window material into the absorption correction. Details on the conversion of transmission to ion-concentration are presented below.

The incident intensity I_0 normalized transmitted intensity I_T (through the entire sample consisting of electrolyte (E) and PEEK windows) can be written as

$$\frac{I_\mathrm{T}}{I_0} = e^{-\mu_\mathrm{PEEK} t_\mathrm{PEEK}} e^{-\mu_\mathrm{E} t_\mathrm{E}}.$$

Equation 4

Here, μ_PEEK and μ_E are the attenuation lengths of the PEEK windows, and the electrolyte, respectively, and $t_\mathrm{PEEK} = 4\ mm$ and $t_\mathrm{E} = 1\ mm$ are the path lengths through the window material and electrolyte channel, respectively.

μ_PEEK was obtained from [12] as

$$\mu_\mathrm{PEEK} = 0.27\ \mathrm{mm}^{-1}.$$

Equation 5

μ_E was measured as

$$\mu_\mathrm{E} = 0.94\ \mathrm{mm}^{-1}.$$

Equation 6

μ_E can be partitioned into contributions from PEO and LiTFSI (here only TFSI was considered due to the negligible absorption of Li)

$$\frac{I_\mathrm{T}}{I_0} = e^{-\mu_\mathrm{PEEK} t_\mathrm{PEEK}} e^{-\mu_\mathrm{PEO} t_\mathrm{PEO}} e^{-\mu_\mathrm{TFSI} t_\mathrm{TFSI}}.$$

Equation 7

We note that we chose to include the linear dependence on concentration in the attenuation coefficients μ in this notation. Using the molar ratio scaled mass attenuation coefficient [13], we arrive at

$$\mu_\mathrm{PEO} = 0.23\mu_\mathrm{E} = 0.22\ \mathrm{mm}^{-1},$$

Equation 8

and

$$\mu_\mathrm{TFSI}^{t=0} = 0.77\mu_\mathrm{E} = 0.72\ \mathrm{mm}^{-1}.$$

Equation 9

We write $\mu_\mathrm{TFSI}^{t=0}$ because the concentration/molar ratio of LiTFSI changes over time.

We now solve Equation 7 for μ_TFSI:

$$\frac{I_\mathrm{T}}{I_0} \frac{1}{e^{-\mu_\mathrm{PEEK} t_\mathrm{PEEK}} e^{-\mu_\mathrm{PEO} t_\mathrm{PEO}}} = e^{-\mu_\mathrm{TFSI} t_\mathrm{TFSI}}$$

Equation 10

256 $$\log\left(\frac{I_\mathrm{T}}{I_0}\frac{1}{e^{-\mu_\mathrm{PEEK}t_\mathrm{PEEK}}e^{-\mu_\mathrm{PEO}t_\mathrm{PEO}}}\right) = -\mu_\mathrm{TFSI}t_\mathrm{TFSI}$$

257 Equation 11

258 $$-\log\left(\frac{I_\mathrm{T}}{I_0}\frac{1}{e^{-\mu_\mathrm{PEEK}t_\mathrm{PEEK}}e^{-\mu_\mathrm{PEO}t_\mathrm{PEO}}}\right)\frac{1}{t_\mathrm{TFSI}} = \mu_\mathrm{TFSI}$$

259 Equation 12

260 Finally, since the attenuation coefficient of a material is proportional to its respective concentration, we
261 can rewrite in terms of the relative TFSI density change $\frac{c_\mathrm{TFSI}}{c_\mathrm{TFSI}^{t=0}}$ with respect to time-dependent μ_TFSI:

262 $$\frac{\mu_\mathrm{TFSI}}{\mu_\mathrm{TFSI}^{t=0}} = \frac{-\log\left(\frac{I_\mathrm{T}}{I_0}\frac{1}{e^{-\mu_\mathrm{PEEK}t_\mathrm{PEEK}}e^{-\mu_\mathrm{PEO}t_\mathrm{PEO}}}\right)\frac{1}{t_\mathrm{TFSI}}}{-\log\left(\frac{I_\mathrm{T}^{t=0}}{I_0}\frac{1}{e^{-\mu_\mathrm{PEEK}t_\mathrm{PEEK}}e^{-\mu_\mathrm{PEO}t_\mathrm{PEO}}}\right)\frac{1}{t_\mathrm{TFSI}}}$$

263 Equation 13

264 $$\frac{c_\mathrm{TFSI}}{c_\mathrm{TFSI}^{t=0}} = \frac{\mu_\mathrm{TFSI}}{\mu_\mathrm{TFSI}^{t=0}} = \frac{-\log\left(\frac{I_\mathrm{T}}{I_0}\frac{1}{e^{-\mu_\mathrm{PEEK}t_\mathrm{PEEK}}e^{-\mu_\mathrm{PEO}t_\mathrm{PEO}}}\right)}{-\log\left(\frac{I_\mathrm{T}^{t=0}}{I_0}\frac{1}{e^{-\mu_\mathrm{PEEK}t_\mathrm{PEEK}}e^{-\mu_\mathrm{PEO}t_\mathrm{PEO}}}\right)} := \frac{c}{c_0}$$

265 Equation 14

266 This assumes that the PEO absorption cross section remains constant, which is justified at it only
267 contributes 23% initially at $t = 0$ and changes less than 20 %.

E. Continuum level transport modelling

We adopted a continuum level model based on concentrated solution theory to describe the characteristics of a Li/PEO-LiTFSI/Li symmetric cell. The mathematical model by Newman and coworkers used in this work is represented as a one-dimensional with a macro-homogenous assumption of electrolyte in a cell. Table S1 summarizes the governing equations. The mass transfer was used to calculate transient concentration profiles across the electrolyte. The ionic potential gradient across the cell can be determined using the modified Ohm's law that includes the effect of concentration gradients in the electrolyte. Butler-Volmer kinetics are used to estimate the charge transfer at the interface between electrode and electrolyte. All transport properties and cell parameters used the values presented in Refs [14, 15] as presented in Table S2 and Table S3. As the transport properties are only available for a few concentration values, we used linear interpolation to determine the transport properties at all concentrations.

In order to calculate the ion velocity, we started with Eq 12.8 and Eq 12.9 from [16], which describes the driving forces of net flux for ion transport due to diffusion, migration and convection as below.

$$N_+ = c_+ \mathrm{v}_+ = -\frac{\nu_+ \mathfrak{D}}{\nu RT}\frac{c_T}{c_0} c \frac{d\mu_e}{dx} + \frac{it_+^0}{z_+ F} + c_+ \mathrm{v}_0$$

Equation 15

$$N_- = c_- \mathrm{v}_- = -\frac{\nu_- \mathfrak{D}}{\nu RT}\frac{c_T}{c_0} c \frac{d\mu_e}{dx} + \frac{it_-^0}{z_- F} + c_- \mathrm{v}_0$$

Equation 16

where N is net flux, v_+ and v_- are the velocity of each ions, c_+ and $c_-$are concentration of each ions, c_T is total concentration ($c_T = c_0 + \nu c$), c_0 is solvent concentration, μ_e is chemical potential of electrolyte, ν is total number of ions, ν_+ and ν_- are the number of each ions and $z_+$and z_- are the charge number of each ions. Note that the solution is electrically neutral, $c = c_+ = c_-$.

Using the relationship between gradient of chemical potential and salt concentration in Eq 12. 13 from [16], we obtain the ion velocity of each species as follow.

$$\mathrm{v}_+ = -D\left(1 - \frac{d\ln c_0}{d\ln c}\right)\frac{dc}{dx}\frac{1}{c_+} + \frac{it_+^0}{z_+ F c_+} + \mathrm{v}_0$$

Equation 17

$$\mathrm{v}_- = -D\left(1 - \frac{d\ln c_0}{d\ln c}\right)\frac{dc}{dx}\frac{1}{c_-} + \frac{it_-^0}{z_- F c_-} + \mathrm{v}_0$$

Equation 18

Note that the solvent velocity, v_0, the driving force of which is convection (either natural, forced, or at high concentrations volume conservation [17, 18]), was assumed as zero in this work. Thus, ion velocity of each species is driven by diffusion and migration forces when the electric field is given in a cell.

Table S1: Summary of governing equations used for Li/PEO-LiTFSI/Li symmetric cell

	Governing equation	Boundary conditions
Mass balance (polymer electrolyte)	$\frac{dc}{dt} = \frac{d}{dx}\left[D\left(1-\frac{d\ln c_0}{d\ln c}\right)\frac{dc}{dx}\right] - \frac{i_2}{F}\frac{dt_+^0}{dx}$ (1)	$-D\left(1-\frac{d\ln c_0}{d\ln c}\right)\frac{dc}{dx}\Big\vert_{x=0} = \frac{(1-t_+^0)}{F} i\vert_{x=0}$ (2) $-D\left(1-\frac{d\ln c_0}{d\ln c}\right)\frac{dc}{dx}\Big\vert_{x=L} = -\frac{(1-t_+^0)}{F} i\vert_{x=L}$ (3)
Modified Ohm's law (Ionic phase)	$i_2 = -\kappa\frac{d\Phi_2}{dx} + \frac{2\kappa RT}{F}\left(1+\frac{d\ln f_\pm}{d\ln c}\right)(1-t_+^0)\frac{d\ln c}{dx}$ (4)	$i\vert_{x=L} = i_0\left[\exp\left(-\frac{\alpha_a F}{RT}\Phi_2\right) - \exp\left(\frac{\alpha_c F}{RT}\Phi_2\right)\right]$ (5) , $\Phi_{1,\ x=L} = 0$
Butler-Volmer equation	$i\vert_{x=0} = i_0\left[\exp\left(\frac{\alpha_a F}{RT}(\Phi_1-\Phi_2)\right) - \exp\left(-\frac{\alpha_c F}{RT}(\Phi_1-\Phi_2)\right)\right]$, $\Phi_{1,\ x=0} = \mathrm{V}_{app}$ (6)	

Table S2: Setting parameters for Li/PEO-LiTFSI/Li symmetric cell

Symbol	parameter	Value	reference
L	thickness of electrolyte	3 mm	measured [14]
κ	ionic conductivity	function of concentration	measured [14]
D	salt diffusion coefficient	function of concentration	measured [14]
t_+^0	cation transference number	function of concentration	measured [14]
F	Faraday's constant	96485 [C/mol]	-
R	universal gas constant	8.314 [J/(mol K)]	-
V_{app}	applied constant voltage	0.3V	
T	operating temperature	90 °C	-

Table S3: Transport properties used for PEO polymer electrolyte with the LiTFSI at 90 °C

r	m (*mol/kg*)	c (*mol/m³*)	D (m²/s)	κ (S/m)	t_+^0 by eNMR Ref. [19]	t_+^0 Ref. [14]	$1+\frac{d\ln\gamma_\pm}{d\ln m}$
0.01	0.23	247	6.0×10^{-12}	2.7×10^{-2}	-	0.07	0.43
0.02	0.45	473	7.8×10^{-12}	7.5×10^{-2}	-	0.23	0.69
0.04	0.91	871	1.0×10^{-11}	1.8×10^{-1}	-	0.40	1.70
0.06	1.36	1200	1.3×10^{-11}	2.0×10^{-1}	0.23	0.33	2.23
0.08	1.82	1590	1.1×10^{-11}	2.2×10^{-1}	-	0.43	3.33
0.10	2.27	1870	8.4×10^{-12}	1.3×10^{-1}	0.19	0.20	2.82
0.12	2.73	2110	7.0×10^{-12}	1.1×10^{-1}	-	0.08	2.78
0.14	3.18	2380	5.8×10^{-12}	9.9×10^{-2}	-	-0.08	2.66
0.16	3.64	2580	9.4×10^{-12}	1.3×10^{-1}	0.15	-0.38	2.27
0.18	4.09	2760	9.0×10^{-12}	1.6×10^{-1}	-	0.10	3.74
0.21	4.77	3050	6.5×10^{-12}	1.2×10^{-1}	-	0.41	6.32
0.24	5.45	3360	6.3×10^{-12}	6.4×10^{-2}	-	0.33	6.00
0.27	6.14	3490	5.9×10^{-12}	4.0×10^{-2}	-	0.18	5.24
0.30	6.82	3780	4.2×10^{-12}	1.5×10^{-2}	-	-0.02	4.49

F. Molecular dynamics simulation

Methodology:

Molecular dynamics (MD) simulations were performed using many-body polarizable APPLE&P force field for PEO, comprised of 64 repeat units at two LiTFSI concentrations corresponding to r = 0.1 and 0.16 (r is the molar ratio between Li^+ and EO). The force field parameters for the LiTFSI force field were taken from previous work [20, 21]. The functional form of the force field is given in Ref. [22]. An archive file with all simulation parameters and MD code used for simulations is attached to the ***Supporting Information*** as a compressed file in tar format. The initial configuration was created by packing solvent and salt in a large box with dimensions of ~150 Å and reducing the box size to 50 Å over 5 ns at 500 K during MD simulations with polarization set to zero and Li^+ and $TFSI^-$ charges reduced by 25% compared to original charge. Subsequently, the polarization was turned on, ion charges were set to their original values and equilibration runs were performed at 423 K for 30 ns for r = 0.1 and 30 - 42 ns for r = 0.16. All other simulation run lengths are tabulated in **Table S4**.

Multiple timestep integrator was employed with 3 timesteps: inner, middle, and outer. An inner timestep was set to 0.5 fs for integration of bonded interactions. A middle time step of 1.5 fs was used for all non-bonded interactions within a truncation distance of 7.0 Å, and an outer timestep of 3.0 fs for all non-bonded interactions between 7.0 Å and the nonbonded truncation distance of 12 Å. The Ewald summation method was used for the electrostatic interactions between permanent charges with other permanent charges or induced dipole moments with k = 6^3 vectors. The reciprocal part of Ewald was calculated every 3.0 fs. Induced dipoles were found self-consistently with convergence criteria of 10^{-9} (electron charge x Å)^2.

Results:

MD simulation predictions are listed in **Table S4**. At r = 0.1, one Li^+ is coordinated by ~5 oxygens of EO and 0.54-0.75 oxygens of $TFSI^-$. The number of oxygens coordinated to $TFSI^-$ decreases and those to EO increases with decreasing temperature in accord with salt dissociation as temperature decreases. Self-diffusion coefficients and ionic conductivity (κ) (see **Equation 19** - **Equation 21**) were extracted a following previously discussed methodology [23], and were in good agreement with pulsed-field gradient (pfg)-NMR measurements as shown in **Figure S7**.

$$\alpha_d = \frac{\kappa}{\kappa_{\text{uncorr.}}}$$

Equation 19

$$\kappa_{\text{uncorr}} = \frac{e^2}{V k_{\text{B}} T}(n_+ D_+ + n_- D_-)$$

Equation 20

$$\kappa = \lim_{t\to\infty} \frac{e^2}{6tVk_{\text{B}}T} \sum_{i,j}^{N} z_i z_j \langle([\mathbf{R}_i(t) - \mathbf{R}_i(0)])([\mathbf{R}_j(t) - \mathbf{R}_j(0)])\rangle$$

Equation 21

where e is the electron charge, V is the volume of the sample, k_{B} is Boltzmann's constant, T is the temperature and n_+ and n_- are the number of Li^+ and $TFSI^-$, respectively. The conductivity calculated without inclusion of ion correlations is denoted as $\kappa_{\mathrm{uncorr.}}$ in **Equation 19**.

At 90 °C, MD simulations predicted conductivity 0.84 mS cm^{-1} for r = 0.1, which is slightly lower than the experimentally measured value of 1.3 mS cm^{-1} [24]. A high degree of dynamic dissociation (ionicity) of 0.88 is in accord with high salt dissociation and experimentally reported values [25].

The Li^+ cation transference number (t^+) was extracted from MD simulations of PEO-LiTFSI (Li:EO = 0.1) following formalism suggested by Wohde et al. [26] based upon Onsager reciprocal relations combined with linear response theory under anion blocking conditions. The full matrix of charge displacements (double sum in **Equation 21**) is decomposed into contributions from cation-cation, cation-anion and anion-anion denoted as κ_{++}, κ_{+-} and κ_{--}. Note that κ_{+-} is defined using the opposite sign from Balabajew et al. [26]. The transference number (t^+) is defined using two parameters α, β, where α characterizes a portion of the positive charge flux if correlations between the Li^+ cations and $TFSI^-$ anions are neglected, while β accounts for correlation between the cation and ion displacements (κ_{+-}) relative to the displacement of the cations (κ_{++}) and anions (κ_{--}). For example, $\beta \rightarrow 1$ corresponds to completely correlated Li^+ and $TFSI^-$ motion such as diffusion of ion pairs. β =0 corresponds to no cation – anion correlations, while $\beta \rightarrow -1$ would be the limit of anticorrelated Li^+ and $TFSI^-$ motion. These parameters (α, β, and t_+) were extracted from the plateaus shown in **Figure S8**. The negative value of β = -0.6 shows moderate anticorrelation of the Li^+ and $TFSI^-$ displacements for both r=0.1 and 0.16 salt concentrations. Hence, we consider our observed β = -0.6 as evidence for moderately anti-correlated cation–anion motion. Thus, as a result of this anti-correlation a positively charged solvent separated $Li^+(EO)_6$ solvate on average moves in the opposite direction from the negatively charged $TFSI^-$, resulting in lower $t^+ = 0.12$ (**Equation 25**) compared to the apparent $t^+_{app} = 0.17$-0.2 (**Equation 26**) that did not include ionic correlation and was extracted from ion self-diffusion coefficients.

$$\alpha = \frac{\kappa_{++}}{\kappa_{++} + \kappa_{--}}$$

Equation 22

$$\beta = \frac{2\kappa_{+-}}{\kappa_{++} + \kappa_{--}}$$

Equation 23

$$\kappa = \kappa_{++} + \kappa_{--}\kappa_{++} + 2\kappa_{+-}$$

Equation 24

$$t^+ = \frac{\beta^2 - 4\alpha + 4\alpha^2}{4(1-\alpha)(\beta - 1)}$$

Equation 25

$$t_{\mathrm{app}}^{+} = \frac{D_{+}}{D_{+} + D_{-}}$$

Equation 26

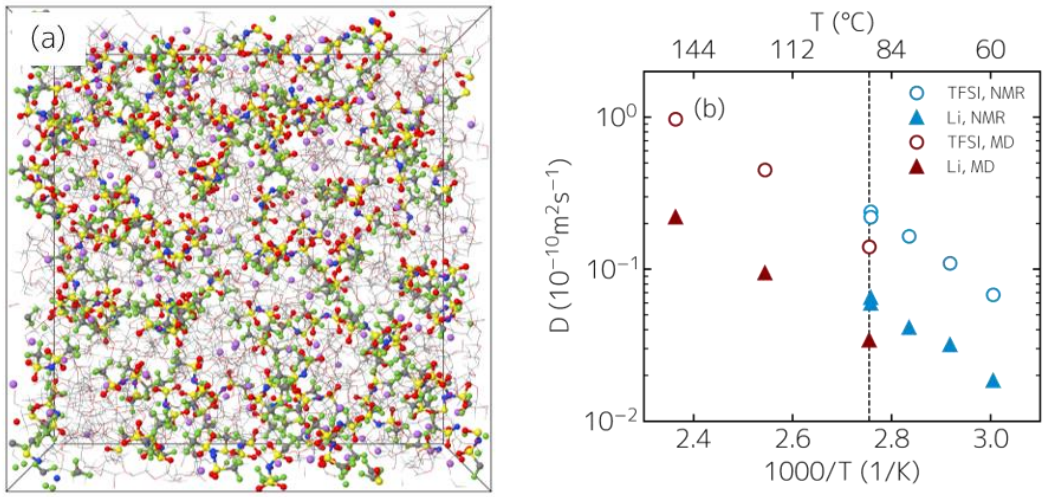

Figure S7: (a) Exemplary snapshot of simulation box; (b) Self-diffusion coefficients of $TFSI^-$ and Li^+ from MD simulations for PEO(Mw=2818)-LiTFSI, r = 0.1 , CH_3-terminated and pfg-NMR PEO(Mw=2480)-LiTFSI, EO:Li=10 CH_3-terminated by Hayamizu et al. [25] and from Pesko et al. [14] PEO(Mw=5kg/mol) OH-terminated at 90 °C; the vertical dashed line indicates 90 °C, the temperature at which both simulation and experiments were performed. The results show good agreement between the NMR- and MD-derived diffusion constants, corroborated from the near-identical slope of log(D) versus 1/T, as well as a difference in the diffusion coefficients at 90 °C less than 2x[27, 28] and accurate predictions of the relative magnitudes of the Li^+ and $TFSI^-$ self-diffusion coefficients.

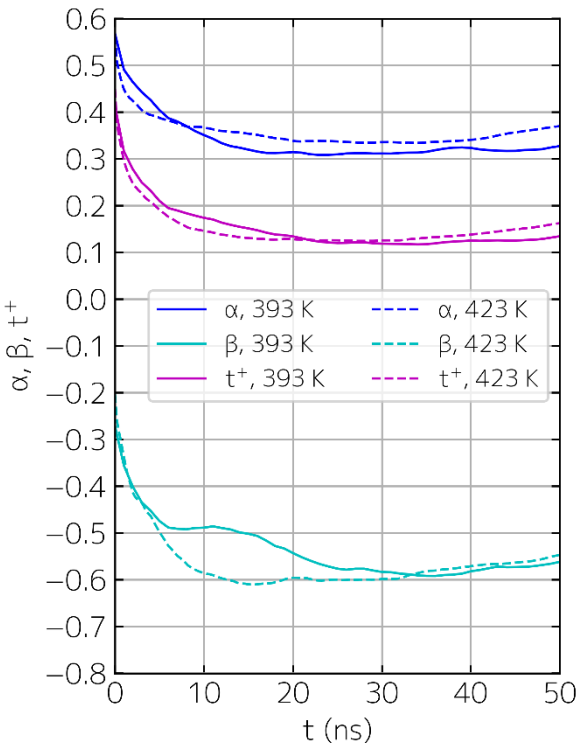

394

395 Figure S8: Running averages for α, β, and t^+ extracted from XY ns MD simulations of PEO-LiTFSI (r = 0.1) at 393 and 423
396 K. Plateaus from 30 – 50 ns and from 20- 40 ns were used to extract parameters after the initial sub-diffusive regime for
397 393 and 423 K, respectively.

398 Table S4: Transport and structural properties for PEO-LiTFSI from MD simulations.

Concentration r:=Li:EO	0.1	0.1	0.1	0.16	0.16	0.16
Temp (K)	423	393	363	423	423	363
Length of equilibration runs (ns)	30	19	76	42	35	27
Length of production runs (ns)	237	116	123	228	263	201
Box (Å)	49.8	49.5	49.2	55.6	55.5	54.9
Density (kg m^{-3})	1249	1273	1299	1334	1339	1387
Diffusion (TFSI) (10^{-10} m^2 s^{-1})	0.97	0.45	0.14	0.62	0.59	0.062
Diffusion (Li) (10^{-10} m^2 s^{-1})	0.22	0.094	0.034	0.18	0.19	0.017
Conductivity (mS cm^{-1})	5.2	2.4	0.84	3.2	3.3	0.51
Degree of dynamic ion dissociation (α_d)	0.96	0.86	0.88	0.64	0.66	0.85
Fraction of free Li (no anion within 5.0 Å)	0.57	0.62	0.64	0.42	0.42	0.50
t^+_{app}, **Equation 26** (comparable to pfg-NMR)	0.18	0.17	0.20	0.23	0.24	0.22
t^+, **Equation 25** (comparable to e-NMR)	0.13	0.12	0.12	0.20	0.17	0.20
Li-EO coordination number (<2.8 Å)	4.73	5.01	5.19	4.05	4.08	4.5
Li-O(TFSI) coordination number (<2.8 Å)	0.75	0.62	0.54	1.28	1.26	1.09
Li-N(OTFSI) coordination number (<5.0 Å)	0.56	0.47	0.42	0.92	0.91	0.79

399

2. Additional figures and text:

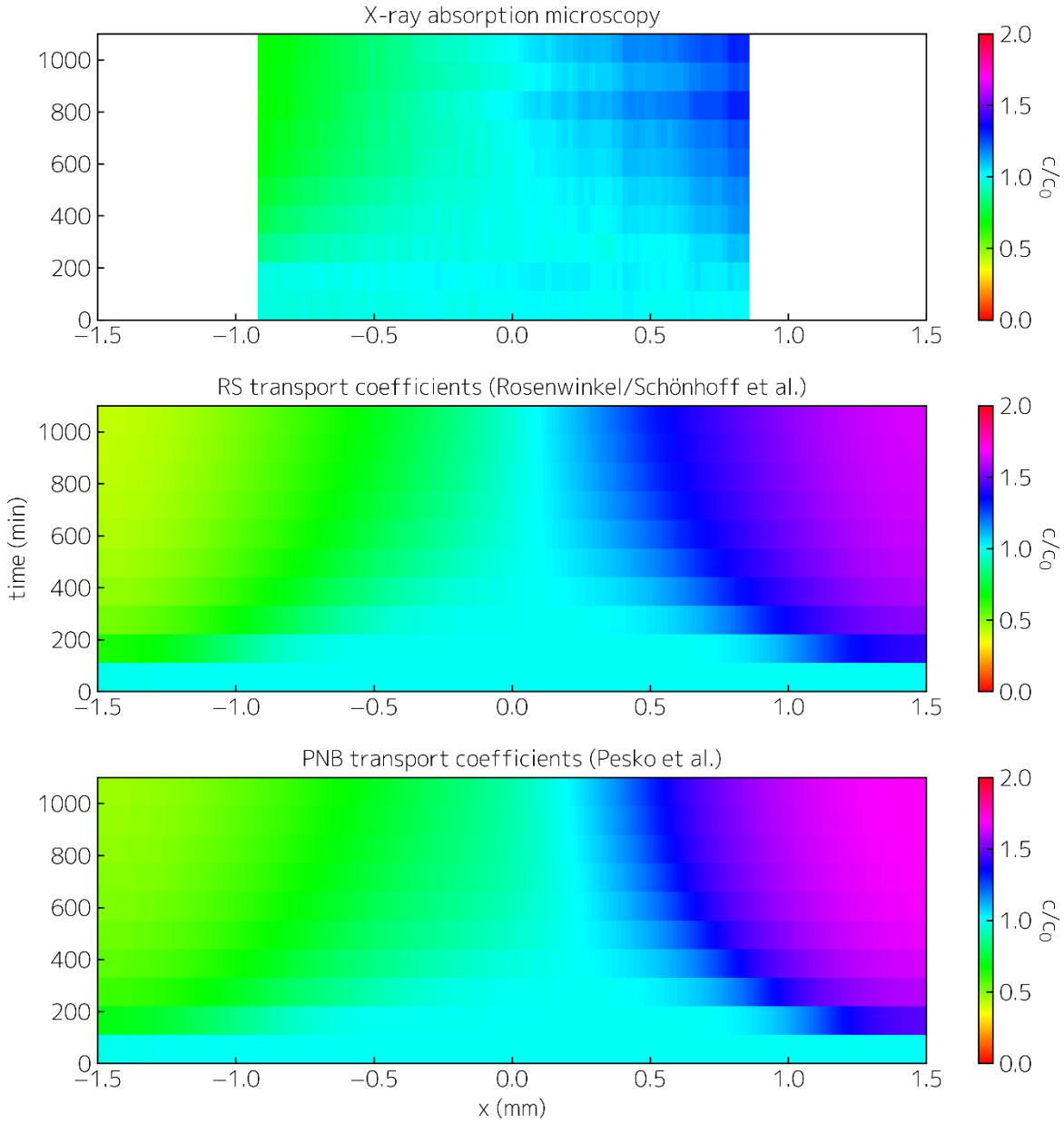

Figure S9: False-color plot of the $TFSI^-$ concentration across 3 mm electrolyte channel (normalized by initial concentration) upon constant voltage (0.3 V) polarization as a function position x and time after polarization. (Top) XAM experiment-derived; (middle) predicted from continuum model under conditions identical to the experiment using RS transport coefficients [19] and (bottom) using PNB transport coefficients [14].

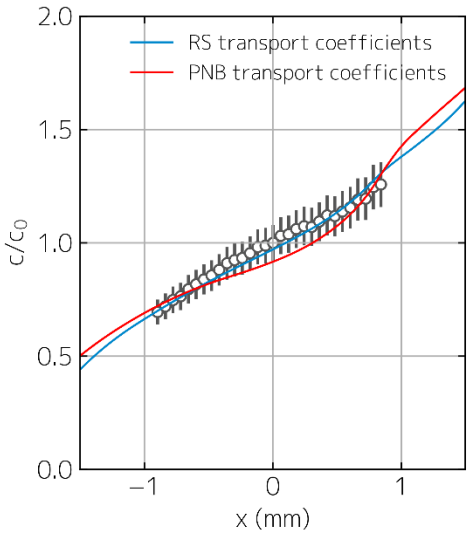

Figure S10: Concentration polarization upon constant voltage (0.3 V) polarization for t= 707 min. Experimental $TFSI^-$ concentration (markers) measured of the Li/LiTFSI-PEO/Li symmetric cell of channel length of 3 mm, and $TFSI^-$ concentration predicted from continuum model under conditions identical to the experiment using RS transport coefficients [19] (blue lines) and using PNB transport coefficients [14] (red).

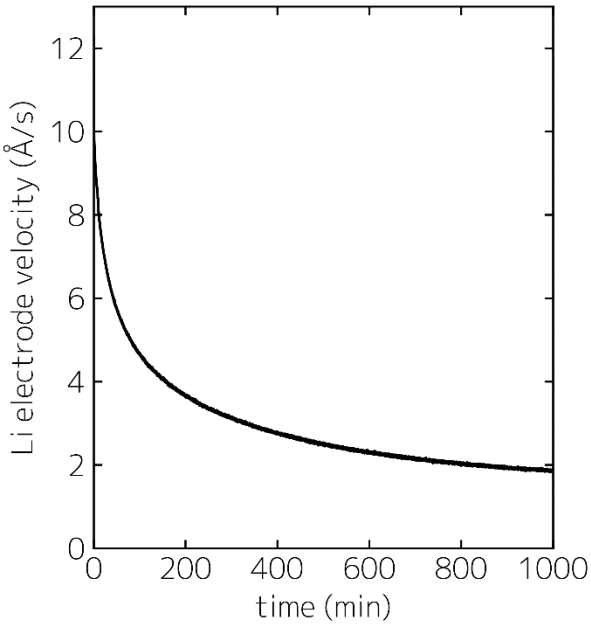

Figure S11: Lithium metal electrode front velocity (due to plating and stripping) as calculated from current density.

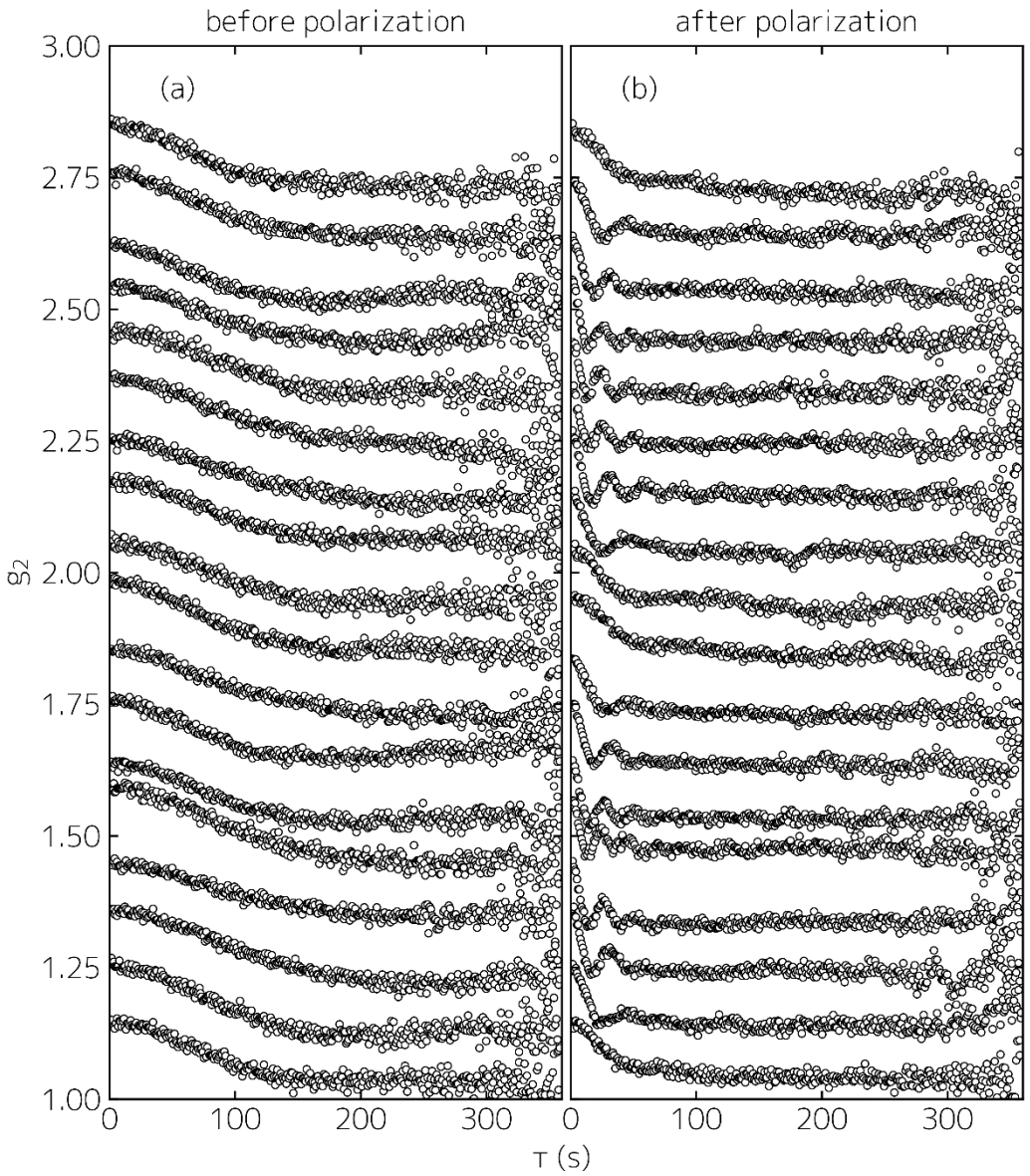

Figure S12: (a) Exemplary measured autocorrelation functions (markers) as a function of delay time τ for different χ-values at a q-value of 0.0038 Å before polarization. (b) same as (a) but after polarization at 0.3 V. The decay time in (a) appears about one order of magnitude slower than in (b) suggesting slower self-dynamics of the LiTFSI/PEO matrix under open circuit equilibrium conditions compared to conditions during ion mass transport.

Microscopic pictorial illustration of the relationship between PEO and $TFSI^-$ velocity

In order to graphically conceptualize the origin behind the observed PEO velocity, we consider a plane located at a random position x between two electrodes, and polymer melt (represented as monomers solvating Li^+ ions) and $TFSI^-$ ions of unity areal size, located directly to the left and to the right of the plane. This scenario is schematically shown in **Figure S13**(a). EO monomers (together with Li ions) are represented by the white boxes and $TFSI^-$ by the green boxes. In this example, an areal (or volumetric in three dimensions) ratio of EO to Li 8:1 was chosen; i.e. for every green $TFSI^-$ box, eight white EO boxes exist. Polarization of the cell will lead to net migration of $TFSI^-$ within the electric field (pointing leftwards in the figure reference). This is shown by the green $TFSI^-$ box moving from the rightwards from **Figure S13**(a) to (b). The jump has two consequences. (1) A void is left behind on the left side of the plane (represented by the red box), and (2) a too crowded situation (orange circle) appears on the right side of the plane, where two monomers and one $TFSI^-$ now take up the space that was previously only being taken up by two monomers. The only compensation for these phenomena is the motion of an EO monomer to the left side of the plane, as seen by the displacement of the white box to fill the void. Now the initial area is occupied by one monomer and one $TFSI^-$ (**Figure S13**(c)). Next, we need to consider how many solvent molecules must move to fill one void. This scales with the volumetric ratios of the solvent and the $TFSI^-$. In the example above, we assumed a volumetric ratio of 8:1. Hence, if one $TFSI^-$ moves, one out of eight EO needs to move, and seven stay stationary. This means that in the ensemble average, the EO velocity is 1/8 times slower than the TFSI (this is equivalent to Equation 3 in the main text).

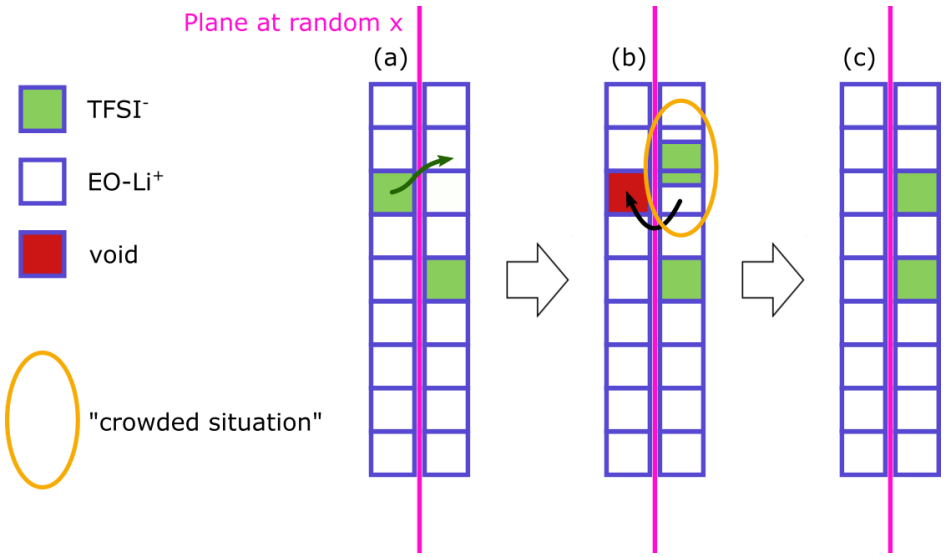

Figure S13: Schematic of microscopic picture of ion transport. (a) During cell polarization, the net drift due to ion migration of Li and $TFSI^-$ from left to right, a $TFSI^-$ unit moves from left to right across the magenta plane. This leads to the situation in (b), where a void is left behind on the left side of the magenta plane, and a "crowded situation" occurs on the right side. This results in the motion of an EO-Li units that make up the same volume as a $TFSI^-$ unit from right to left filling the void.

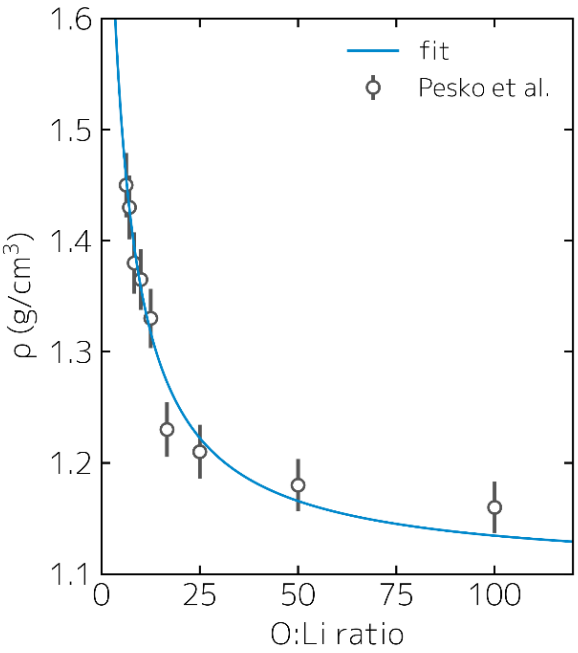

Figure S14: Concentration dependence of the mass density of LiTFSI in PEO. The experimental values are from Pesko et al. [14] and the solid line is a fit to $\boldsymbol{\rho} = \frac{\boldsymbol{M_{\mathrm{LiTFSI}}+(M_{EO}/r)}}{\boldsymbol{V_{\mathrm{LiTFSI}}+(V_{EO}/r)}}$.

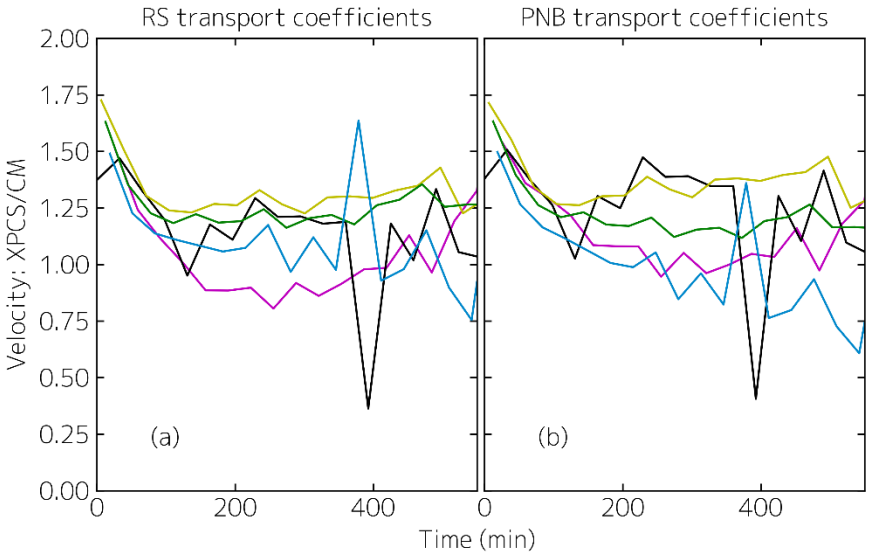

Figure S15: Ion velocities. (a) XPCS-calculated TFSI velocity for different locations within cell (color-code corresponding to Figure 5 (main text)) measured upon constant voltage (0.3 V) polarization of the Li/LiTFSI-PEO/Li symmetric cell of channel length of 3 mm as a function of time, divided by the TFSI velocity predicted from continuum model under conditions identical to the experiment using RS transport coefficients [19] and using PNB transport coefficients [14].

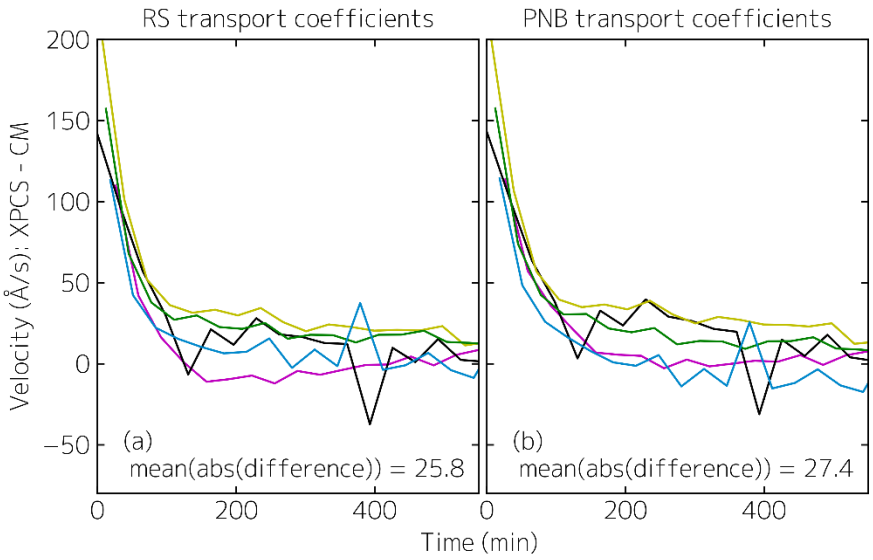

Figure S16: Ion velocities. (a) XPCS-derived TFSI velocity for different locations within cell (color-code corresponding to Figure 5 (main text) measured upon constant voltage (0.3 V) polarization of the Li/LiTFSI-PEO/Li symmetric cell of channel length of 3 mm as a function of time, subtracted by the TFSI velocity predicted from continuum model under conditions identical to the experiment using RS transport coefficients [19] and using PNB transport coefficients [14].

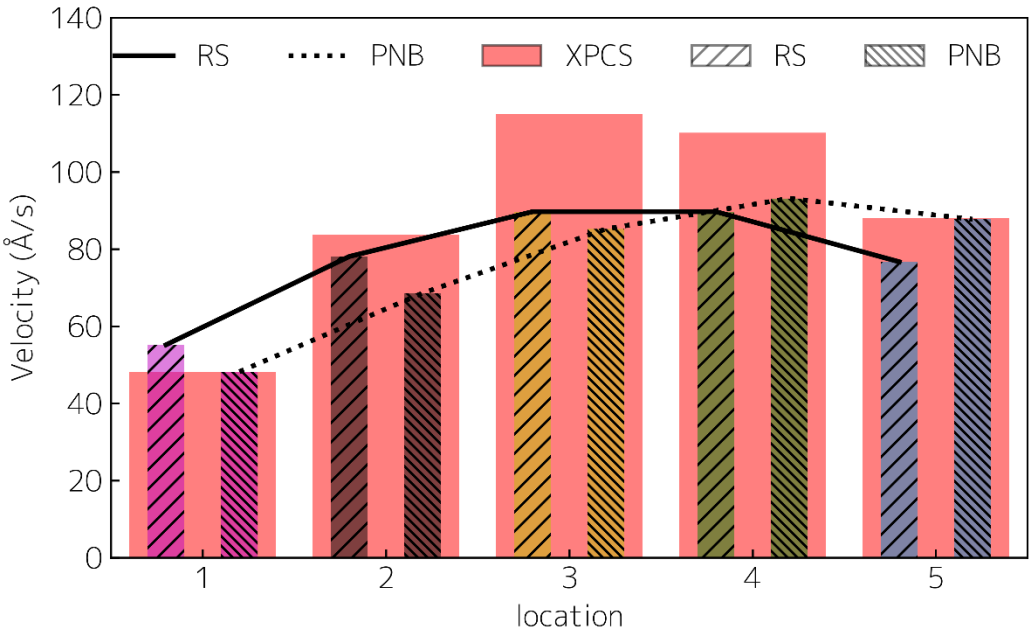

Figure S17: XPCS measured and continuum model simulated (using RS transport coefficients [19] and PNB transport coefficients [14]) $TFSI^-$ velocity for different locations within cell (color-code corresponding to Figure 5 (main text)) measured upon constant voltage (0.3 V) polarization of the Li/LiTFSI-PEO/Li symmetric cell of channel length of 3 mm averaged for polarization times $200 < t < 400$ min. The agreement in the location dependence between measurements and simulation is more consistent with the RS transport coefficients (solid line) compared to the PNB transport coefficients (dotted line) as evident by the smaller spread in deviation and the more symmetric distribution around location 3 (center of cell) (similar to experiment).

References

1. A. R. Sandy, L. B. Lurio, S. G. J. Mochrie, A. Malik, G. B. Stephenson, J. F. Pelletier and M. Sutton, *Journal of Synchrotron Radiation*, 1999, **6**, 1174-1184.
2. F. Khan, S. Narayanan, R. Sersted, N. Schwarz and A. Sandy, *J Synchrotron Radiat*, 2018, **25**, 1135-1143.
3. M. Sutton, K. Laaziri, F. Livet and F. Bley, *Opt Express*, 2003, **11**, 2268-2277.
4. G. Grübel, A. Madsen and A. Robert, *Soft Matter Characterization*, 2008, DOI: 10.1007/978-1-4020-4465-6_13, 953-995.
5. M. Sutton, *Comptes Rendus Physique*, 2008, **9**, 657-667.
6. B. J. Berne and R. Pecora, *Dynamic light scattering: with applications to chemistry, biology, and physics*, Courier Corporation, 2000.
7. F. Livet, F. Bley, F. Ehrburger-Dolle, I. Morfin, E. Geissler and M. Sutton, *Journal of Synchrotron Radiation*, 2006, **13**, 453-458.
8. J. R. M. Lhermitte, M. C. Rogers, S. Manet and M. Sutton, *Review of Scientific Instruments*, 2017, **88**, 0-7.
9. O. Oparaji, S. Narayanan, A. Sandy, S. Ramakrishnan and D. Hallinan, *Macromolecules*, 2018, **51**, 2591-2603.
10. J. Lhermitte, McGill University, 2015.
11. M. Newville, T. Stensitzki, D. B. Allen, M. Rawlik, A. Ingargiola and A. Nelson, *Astrophysics Source Code Library*, 2016.
12. B. Henke, *Journal*.
13. L. Gerward, N. Guilbert, K. B. Jensen and H. Levring, *Radiation Physics and Chemistry*, 2001, **60**, 23-24.
14. D. M. Pesko, K. Timachova, R. Bhattacharya, M. C. Smith, I. Villaluenga, J. Newman and N. P. Balsara, *Journal of the Electrochemical Society*, 2017, **164**, E3569-E3575.
15. D. M. Pesko, Z. Feng, S. Sawhney, J. Newman, V. Srinivasan and N. P. Balsara, *Journal of The Electrochemical Society*, 2018, **165**, A3186-A3194.
16. J. Newman and K. E. Thomas-Alyea, *Electrochemical systems*, John Wiley & Sons, 2012.
17. A. Ehrl, J. Landesfeind, W. A. Wall and H. A. Gasteiger, *Journal of The Electrochemical Society*, 2017, **164**, A826-A836.
18. A. J. Ehrl, TU Munich, 2017.
19. M. P. Rosenwinkel and M. Schönhoff, *Journal of The Electrochemical Society*, 2019, **166**, A1977-A1983.
20. O. Borodin, L. Suo, M. Gobet, X. Ren, F. Wang, A. Faraone, J. Peng, M. Olguin, M. Schroeder, M. S. Ding, E. Gobrogge, A. von Wald Cresce, S. Munoz, J. A. Dura, S. Greenbaum, C. Wang and K. Xu, *ACS Nano*, 2017, **11**, 10462-10471.
21. L. Suo, O. Borodin, T. Gao, M. Olguin, J. Ho, X. Fan, C. Luo, C. Wang and K. Xu, *Science*, 2015, **350**, 938-943.
22. O. Borodin, *J. Phys. Chem. B*, 2009, **113**, 11463-11478.
23. O. Borodin and G. D. Smith, *Macromolecules*, 2006, **39**, 1620-1629.
24. D. M. Pesko, K. Timachova, R. Bhattacharya, M. C. Smith, I. Villaluenga, J. Newman and N. P. Balsara, *J. Electrochemical Soc.*, 2017, **164**, E3569-E3575.
25. K. Hayamizu, E. Akiba, T. Bando and Y. Aihara, *J. Chem. Phys.*, 2002, **117**, 5929-5939.
26. F. Wohde, M. Balabajew and B. Roling, *Journal of The Electrochemical Society*, 2016, **163**, A714-A721.
27. D. J. Brooks, B. V. Merinov, W. A. Goddard, B. Kozinsky and J. Mailoa, *Macromolecules*, 2018, **51**, 8987-8995.
28. N. Molinari, J. P. Mailoa and B. Kozinsky, *Chemistry of Materials*, 2018, **30**, 6298-6306.

520